Accurate holographic cytometry using three-dimensional hydrodynamic focusing

IOP Publishing Journal of Micromechanics and Microengineering
J. Micromech. Microeng. **33** (2023) 024003 (10pp) https://doi.org/10.1088/1361-6439/acad0f

Accurate holographic cytometry using three-dimensional hydrodynamic focusing

Yogesh M Patel[1], Ritika Malik[2], Kedar Khare[2,3] and Supreet Singh Bahga[1,*]

[1] Department of Mechanical Engineering, Indian Institute of Technology Delhi, New Delhi 110016, India
[2] Department of Physics, Indian Institute of Technology Delhi, New Delhi 110016, India
[3] Optics and Photonics Centre, Indian Institute of Technology Delhi, New Delhi 110016, India

E-mail: bahga@mech.iitd.ac.in

Received 12 October 2022, revised 8 December 2022
Accepted for publication 20 December 2022
Published 3 January 2023

Abstract

We present a microfluidic holographic cytometry technique using three-dimensional (3D) hydrodynamic focusing for accurate visualization, classification, and quantification of the cells and particles from a mixture. Our approach uses high-resolution, single-shot digital holographic microscopy to image moving cells and particles in a specially-designed microfluidic device that orders the cells and particles in a single file close to the bottom wall of the channel. Our 3D-focusing microfluidic device allows high-magnification holographic imaging without the need for computationally-expensive numerical refocusing used by the existing holographic cytometry techniques. Our microfluidic device also prevents the clustering of cells and can be fabricated at a low-cost using micromilling. To demonstrate the efficacy of our method, we consider a challenging case of classification from a mixture of unstained red blood cells and polystyrene particles, which are otherwise indistinguishable in brightfield and phase-contrast microscopy. Through experiments with cell-particle mixtures with varying proportions, we show that our holographic cytometry technique can precisely count and classify the cells and particles based on their reconstructed phase values. Our holographic cytometry technique has the potential for label-free classification and quantification of infected cells for applications such as disease diagnostics, cancer research, and genomics.

Supplementary material for this article is available online

Keywords: digital holographic microscopy, hydrodynamic focusing, imaging flow cytometry, microfluidics

(Some figures may appear in colour only in the online journal)

1. Introduction

Imaging flow cytometry (IFC) is a hybrid technique that integrates microfluidic flow cytometry with optical microscopy for quantitative high-resolution digital imaging of a large number of cells. IFC has found applications in various fields, including personalized medicine, clinical diagnosis assessment, and cell phenotype profiling [1–4]. The integration of microscopy with a flow cytometer has several advantages compared with the single-point detection method. Firstly, imaging allows the characterization of cell morphology, which is vital in evaluating and diagnosing numerous diseases. Moreover, unlike traditional flow cytometers, microfluidic IFC involves minimal

* Author to whom any correspondence should be addressed.

sample and reagent consumption, lesser unit cost, and minimal contamination by using disposable microfluidic devices. Various optical imaging techniques have been demonstrated for IFC of cells and particles, such as leukemic cells [2], endothelial cells [4], breast cancer cells [5], epithelial cells [6], carcinoma cells [6], latex beads [7], and leukocytes [8]. Amongst all, fluorescence and brightfield microscopy are the most commonly used techniques for imaging in IFC [1–11]. Even though brightfield microscopy is widely used for cell imaging, low contrast limits its applicability for detailed analysis of cellular features [12]. On the other hand, fluorescence microscopy allows precise identification of cells based on the specific wavelengths emitted by fluorophores attached to individual particles or cells. Fluorescence tagging of cells not only requires additional wet-lab processing effort but also renders the cells unviable for further analysis. Therefore, there is a need for high-resolution label-free imaging of cells in IFC.

Digital holographic microscopy (DHM) has emerged as a high-resolution imaging technique that can quantify cellular characteristics without fluorescent tagging [13]. DHM differs from traditional microscopy techniques because it does not directly record a visually meaningful image of the object [14]. Instead, the object's light wavefront data is digitally captured as a hologram, and after that, the object image is reconstructed using a numerical method [15]. Consequently, rather than modifying the bright field image with phase shift information as in a phase contrast microscope, DHM generates a quantitative phase image, which provides the optical thickness of the object. The optical thickness depends on the thickness and refractive index of the objects, such as cells and particles. Hence, cells and particles of the same morphology but having different refractive indices can be recognized in DHM, which are otherwise indistinguishable in brightfield and phase-contrast microscopy.

The application of DHM for label-free classification of cells in IFC has been recently demonstrated in a few microfluidic devices. Zetsche *et al* [16] used DHM to classify planktonic cells flowing in a straight microfluidic channel based on their morphological and textural features. Later, Mandracchia *et al* [17] demonstrated volumetric counting of the red blood cells in a single microfluidic channel using DHM. Xin *et al* [18] accessed the drug resistance of ovarian cancer cells by extracting the optical, morphological, and textural features from quantitative phase images of cells flowing in a straight microchannel. In the aforementioned demonstrations of DHM in IFC, the cells were made to flow in a straight microfluidic channel. Consequently, the cells were randomly distributed throughout the depth of the microfluidic channel and hence required numerical refocusing [16–18]. Such numerical refocusing involves propagating the reconstructed complex-valued object field from the hologram in small steps ($\sim 1\,\mu$m) over the whole channel depth ($\sim 100\,\mu$m). The best focus plane is then determined by applying some sharpness or contrast metric to complex-valued fields in all the propagated planes [19, 20]. The numerical propagation of object fields recovered from a hologram and focus plane determination thus require a few hundred fast Fourier transform and image gradient operations for an individual object (cell or particle). The numerical reconstruction along with focus plane detection in DHM thus requires much more additional computational resources. Moreover, if an individual object is far from the nominal plane that is in focus while recording the digital hologram, the corresponding object field may be highly blurred, and there is a possibility of missing such objects completely. To reduce the number of steps in numerical refocusing algorithms, Chen *et al* [21] and Park *et al* [22] performed DHM-based IFC in a shallow microchannel. Although the use of a shallow microchannel, which requires an expensive microfabrication process, reduced the numerical refocusing steps, the experiments of Park *et al* [22] showed that it did not prevent the cells from clustering.

To improve the cell counting and classification accuracy of DHM-based IFC, it is necessary to use a microfluidic device that prevents cell-clustering and allows high-magnification imaging of cells in a single focal plane. Moreover, it is desirable to have an inexpensive microfluidic device because, in practice, the microfluidic chips for cytometry need to be disposed off after single use to avoid contamination. To this end, we here demonstrate an alternate way of holographic cytometry for accurate cell counting and classification without the need for computationally expensive numerical refocusing and resource-intensive microfabrication processes. In this work, we present microfluidic holographic cytometry using three-dimensional (3D) hydrodynamic focusing as a convenient, label-free method for the accurate classification and counting of cells and particles. We image individual unstained RBCs and polystyrene particles using an inverted, single-shot DHM setup that is integrated with an inexpensive microfluidic device fabricated in poly(methyl methacrylate) (PMMA) using micro milling. Our microfluidic device employs 3D hydrodynamic focusing of the cells and particles in a single-file arrangement near the bottom wall of the device. As all the cells and particles remain in the focal plane, our method does not require numerical refocusing as needed by all previous works on DHM-based IFC. Moreover, positioning the cells near the bottom wall of the channel allows imaging with high magnification and low working distance microscope objectives. By imaging RBCs and polystyrene particles, we demonstrate the ability of DHM along with our inexpensive 3D-focusing microfluidic device for accurate counting and classification of cells and particles in IFC, without the need for numerical refocusing.

We begin by demonstrating the ability of DHM to classify stationary, unstained red blood cells and polystyrene particles based on the reconstructed phase values. Thereafter, we report the working principle and fabrication of our inexpensive 3D hydrodynamic focusing microfluidic chip. We also discuss the choice of geometric and operational parameters through computational fluid dynamics simulations. We then demonstrate the visualization of cells and particles in the 3D hydrodynamic focusing device using DHM. Finally, we report the counting

and classification of cells and particles from mixtures with varying proportions of cells and particles using DHM-based IFC.

2. Imaging cytometry using DHM

2.1. DHM visualization of stationary cells and particles

The schematic diagram of the inverted DHM setup for label-free imaging of biological cells and particles is illustrated in figure 1(A). The DHM technique is based on interference between two phase-differentiated coherent beams, the object, and the reference beams [23]. The object beam travels through the cells and particles while the reference beam remains undisturbed. An interference pattern (hologram) is generated when the object beam merges with the reference beam. The interference pattern, which consists of the amplitude and phase of the entire image field, is recorded by a camera. This interference pattern carries the entire depth information of cells and particles.

The phase recovered from the interferometric pattern is expressed mathematically by the arctangent function, which is wrapped in the interval $[-\pi, \pi]$. Thus, phase unwrapping is required to associate a particular phase map with a surface profile (cell and particle), which is carried out by using the transport of intensity equation based method [24]. Moreover, the phase profile information is reconstructed from the interferometric pattern using an optimization-based numerical method described by Singh and Khare [25]. The magnitude of phase shift is regulated by the optical thickness, which depends on the thickness and refractive index of the cells and particles. The unwrapped phase map can be related to the morphology of the object (cell or particle) as follows: $\phi(x,y) = (2\pi/\lambda) \int \mathrm{d}z\ n_{\mathrm{r}}(x,y,z)$. Here λ is the illumination laser wavelength, and $n_{\mathrm{r}}(x,y,z)$ is the real part of the relative refractive index profile of the cells and particles with respect to the surrounding medium. The imaginary part of the refractive index generally refers to the absorption coefficient which is negligible for unstained transparent objects used here. The maximum phase is calculated by taking the maximum value in a particular phase profile (cells and particles) within the region of interest (ROI), $\phi_{\max} = \max_{x,y} \phi(x,y)$. The phase map computed through the holographic technique also contains additional morphological information which was not required in the present demonstration, however, may be useful in the future for other objects that may possess internal structure. Note that our optimization based numerical approach allows phase reconstruction with full diffraction-limited resolution from a single image of the interference pattern as shown in section 2.4. This single-shot DHM capability allows us to reconstruct phase of moving cells and particles.

We used a DHM system (Holmarc, HO-DHM-UT01, India) based on the Mach–Zehnder interferometer, as shown in figure 1(A), to measure the relative phase shift. Here, beam splitter 1 splits the low-intensity collimated laser beam ($\lambda =$ 633 nm, 3 mW) into two parts. Thereafter, a slight incline in beam splitter 2 yields a slanted plane reference beam $R(x,y)$ and an enlarged image field $O(x,y)$ at the sensor plane using the infinity imaging system. In our setup, a white LED is also provided separately so that the sample slide plane can be imaged onto the sensor in bright field mode.

Previous works on DHM-based IFC used morphological features, such as cell size and shape, in addition to DHM-derived phase values for cell classification in IFC [16, 18, 22]. In contrast, for our experiments, we considered a challenging case of classification from a mixture of morphologically-similar unstained RBCs and 10 μm particles in 1× phosphate-buffered saline (PBS) solution. These unstained cells and particles were chosen purposefully because they are indistinguishable under brightfield and phase-contrast microscopy and can be classified only on the basis of their phase values.

First, we visualized the individual cells and particles and a mixture of cells and particles on glass slides in brightfield mode using an inverted microscope equipped with a 20× objective (NA = 0.45, Plan Fluor) and a CMOS camera (uEye 3070 CP, IDS, Germany). The brightfield microscopy images of the unstained RBCs, particles and the mixture of RBCs and particles are shown in figures 1(a)–(c), respectively. These images clearly show that the unstained RBCs and particles are difficult to distinguish using a brightfield microscope. In the supporting information, we show that these cells and particles are even indistinguishable using phase-contrast microscopy. Next, we visualized the cells and particles using the same microscopy setup but in the holographic mode. The interference patterns captured for individual RBCs, particles, and the mixture of RBCs and particles are shown in figures 1(d)–(f), respectively. Figures 1(g)–(i) show the reconstructed phase image of individual RBCs, individual particles, and a mixture of RBCs and particles. The cells and particles show a clear quantitative difference in their phase profiles. Hence, we infer that DHM can recognize the cells and particles based on the phase value, which are otherwise indistinguishable in brightfield microscopy. The maximum phase, $\phi_{\max}$ for cells is in the range of 3.0–4.0 rad, whereas the maximum phase of particles ranges between 6.3 and 7.0 rad.

2.2. Microfluidic device design

2.2.1. Working principle and fabrication. We designed and fabricated an IFC microfluidic device, which is particularly suitable for high-magnification DHM-based cell imaging and counting while avoiding numerical refocusing. The design of the microfluidic device is shown schematically in figure 2. The cross-junction microdevice consists of one sample inlet, two sheath inlets, and one outlet. The mixture of cells and particles is injected into the device from the sample channel while sheath fluid is introduced from the sheath channels. At the junction, the sheath fluid hydrodynamically focuses the cells and particles along the width of the channel. A novel feature of the device is that the height of the sheath channels is kept greater than that of the sample channel so that the sheath fluid also focuses the cells and particles along the depth of

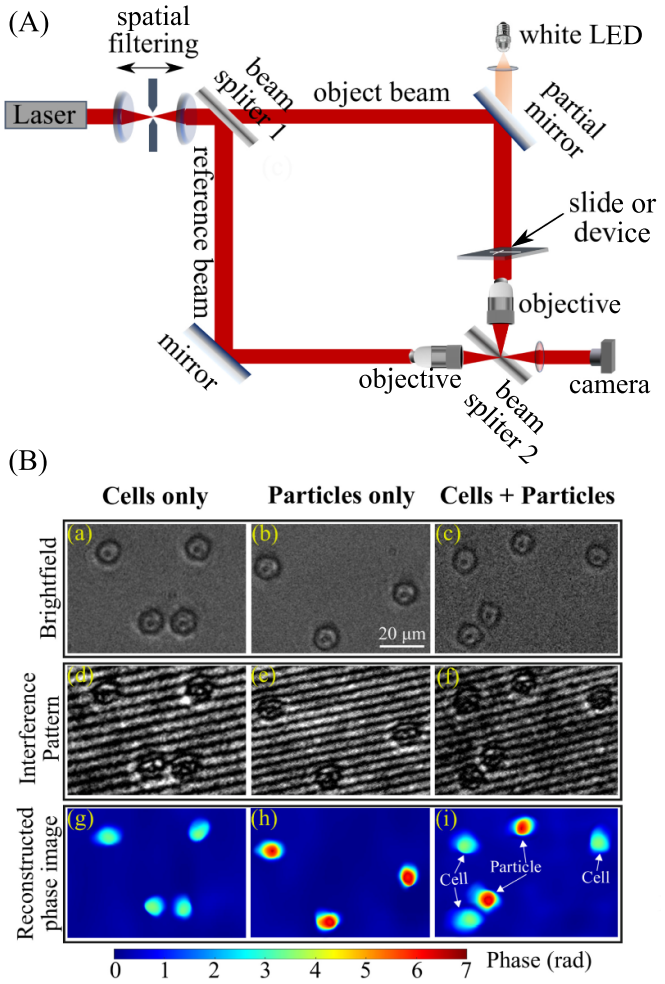

Figure 1. (A) Schematic representation of an inverted DHM system based on the Mach–Zehnder configuration. (B) Reconstruction of the phase profile from the interference patterns. Brightfield images of (a) unstained RBCs (b) polystyrene particles (c) mixture of RBCs and particles. Interference patterns for (d) RBCs (e) polystyrene particles (f) mixture of RBCs and particles. Reconstructed phase images of (g) RBCs (h) polystyrene particles (i) mixture of RBCs and particles. The chosen cells and particles are indistinguishable under a brightfield microscope (a)–(c). However, after reconstructing the phase profile (g)–(i), it is possible to differentiate the same-sized cells and particles.

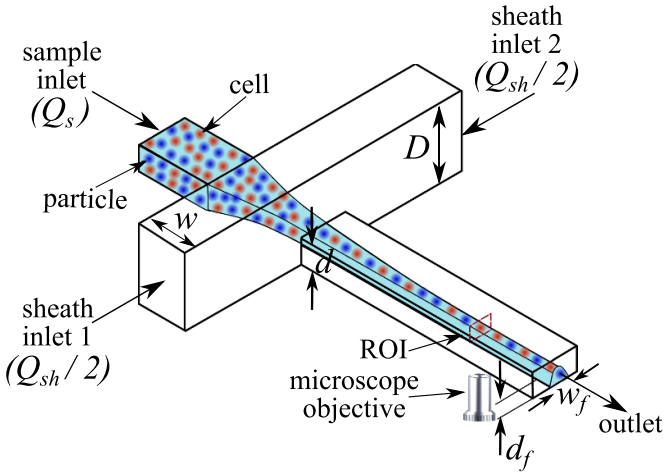

Figure 2. Schematic of the microfluidic chip for IFC. A mixture of cells and particles are three-dimensional (3D) hydrodynamically focused close to the bottom wall downstream of the cross-junction as the height of the sheath channel is higher than the height of the sample channel that connects the sample inlet and outlet.

the channel, resulting in 3D focusing of cells and particles. Unlike other 3D sheath flow focusing devices, our specially-designed device focuses the cells in a single file close to the bottom wall of the microchannel. Hence, our device ensures the alignment of the cells and particles within the small working distance of the high-magnification objective of the inverted digital holographic microscope. More importantly, the cells and particles flow within the depth-of-field of the microscope objectives, thereby avoiding the need for computationally-expensive numerical refocusing in DHM.

The microfluidic device was fabricated on a 3 mm thick PMMA substrate using micro milling with a 200 μm diameter carbide endmill. After that, the reservoirs at the channel ends were made by drilling 2 mm diameter holes. The open microfluidic device was cleaned with de-ionized water and isopropyl alcohol and then thermally bonded with a 250 μm thick PMMA sheet. In the present study, the widths (w) of all the channels were 200 μm, while the height of the sheath channels (D) and main channel (d) were 300 μm and 100 μm, respectively. This height ratio D/d was chosen based on numerical simulations, discussed in section 2.2.2. The sample channel connecting the sample inlet and outlet was 35 mm long, while the sheath channel was 15 mm long. Moreover, the distance between the inlet reservoirs to the cross-junction was 7.5 mm, whereas the distance between the outlet and cross-junction was 27.5 mm in our fabricated chip.

2.2.2. Numerical simulations of three-dimensional hydrodynamic focusing. To design and assess the effectiveness of the device for 3D flow focusing of the sample stream, we performed 3D computational fluid dynamics simulations. The depth (d_f) and width (w_f) of focused sample stream are governed by the dimension of the device (w, D, d) and flow rate of the sample (Q_s) and sheath fluids (Q_{sh}). At low Reynolds number, the dimensionless depth (d_f/d) and width (w_f/w) of the focused stream depend primarily on three dimensionless numbers, (a) height ratio of the sheath-to-sample channels (D/d), (b) aspect ratio of the sample channel (w/d), and (c) sample-to-sheath flow rate ratio (Q_s/Q_{sh}). To investigate the effect of the D/d and the Q_s/Q_{sh} on the w_f/w and d_f/d, we solved the mass and momentum conservation equations for the steady, incompressible flow using a commercial computational package (COMSOL Multiphysics). The computational domain, shown in figure 3(a) has the same geometrical dimensions as the actual device. We applied uniform velocity boundary conditions at the sample and sheath inlets, while constant pressure boundary condition was prescribed at the outlet as

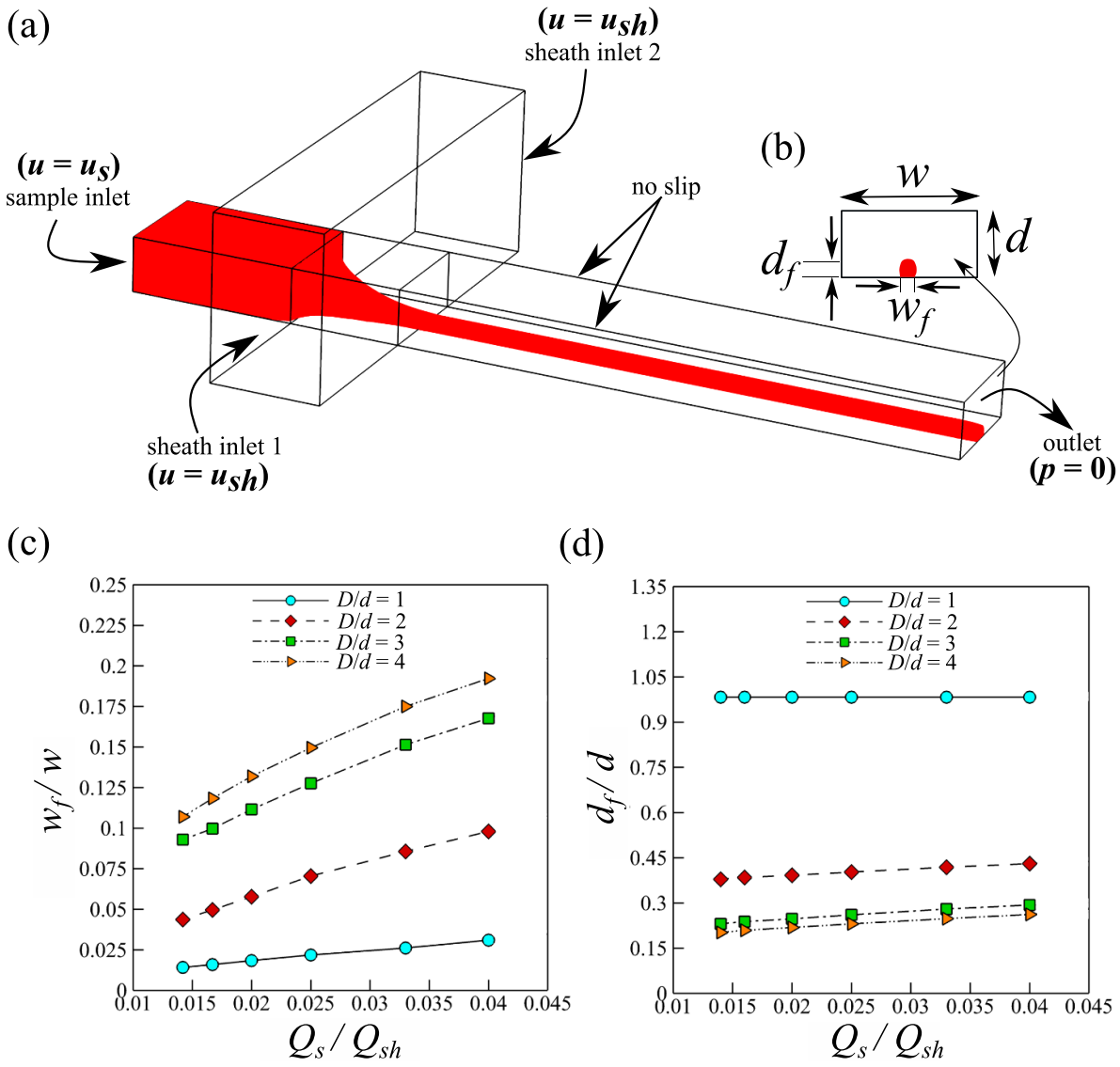

Figure 3. (a) Simulated 3D hydrodynamic focusing of sample stream for height ratio $D/d = 3$ and flow rate ratio $Q_s/Q_{sh} = 0.025$. (b) Cross-section of the 3D-focused stream at the outlet of the microchip. The streamlines originating from the sample inlet were computed to calculate the width and depth of the hydrodynamically focused stream. (c), (d) Numerically predicted width and depth of the focused stream for various combinations of D/d and Q_s/Q_{sh}. The depth of the focused stream (d_f) can be varied primarily by D/d, while the desired width (w_f) can be achieved by controlling Q_s/Q_{sh}.

shown in figure 3(a). The no-slip boundary condition was used at all walls of the microchannel. We used the uniform quadrilateral grid in the x, y, and z directions. The simulations were performed for various mesh sizes ranging from 0.43 μm to 0.01 μm. Based on the grid independence test, we selected a mesh size of 0.04 μm for the numerical investigation of fluid flow in a flow-focusing device.

The streamlines starting from the sample inlet were computed to calculate the depth and width of the hydrodynamically focused stream. The extreme streamlines at the outlet of the microfluidic chip were used to estimate the depth and width of the focused stream, as shown in figures 3(a) and (b). The simulated width and depth of the focused sample stream for varying flow rate ratio (Q_s/Q_{sh}), and the height ratio (D/d) are presented in figures 3(c) and (d). We infer from figure 3(c) that the width of the focused stream reduces almost linearly upon decreasing Q_s/Q_{sh}. This is because at lower Q_s/Q_{sh}, a larger fraction of the sheath fluid is available to focus the sample fluid. As shown in figure 3(a), for $D/d > 1$, the sample stream focuses three-dimensionally close to the bottom wall of the microchannel. Figures 3(c) and (d) shows that as the D/d increases, the depth of focused stream reduces. However for increasing height ratio (D/d), the width of the focused stream increases to ensure mass continuity of the sample stream.

From figure 3(d), we also infer that the depth of the focused stream is weakly dependent on the sample-to-sheath flow rate ratio and mainly dependent on the height ratio of the sheath-to-sample channels. Therefore, to get desired depth (d_f/d) of the

focused stream, firstly, the height ratio of the sheath-to-sample channels (D/d) can be fixed. Subsequently, the sample-to-sheath flow rate ratio (Q_s/Q_{sh}) can be selected to achieve the desired width (w_f/w) of the sample stream without varying the depth of the focused stream. Hence, our device enables independent control of the depth and width of the focused stream by the height ratio of the sheath-to-sample channels (D/d) and sample-to-sheath flow rate ratio (Q_s/Q_{sh}), respectively. This unique characteristic of our 3D hydrodynamic focusing chip is beneficial for the easy selection of operating parameters and device dimensions to focus cells and particles of different sizes. Moreover, as suggested by the simulations, our 3D sheathing technique is not restricted to a specific range of flow rates. Therefore, our microfluidic chip can be operated at even higher flow rates for high-throughput cytometry systems. Based on simulations, we estimated that for $D/d = 3$ and $Q_s/Q_{sh} = 0.025$, both the depth (d_f) and the width of the focused (w_f) stream in our device are around 25 μm, which are approximately three times the diameter of cells or particles. Our experiments presented in section 2.3 show that this combination of D/d and Q_s/Q_{sh} ensures accurate 3D hydrodynamic focusing of cells, which prevents cell-clustering and obviates the need for numerical refocusing along the depth of the microchannel.

2.3. Experimental methodology

Figure 4(a) shows a schematic illustration of the experimental setup for visualization and classification of a large number of cells and particles from the mixture. In all sets of experiments, the sample fluid consists of cells (RBCs) and particles (polystyrene, 10 μm, Sigma-Aldrich) mixed in 1× PBS solution, while the sheath fluid was 1× PBS buffer. A single-channel syringe pump (KD Scientific/Cole-Parmer, Legato 110, USA) was used to inject the sample fluid, while a dual-channel syringe pump (KD Scientific, Legato 210, USA) was used to inject the sheath fluid from the two side channels. The syringes containing the sheath and sample fluids were connected to the inlet reservoirs using pressure monitoring tubes, as shown in the figure 4(b). At a cross-junction, the sheath fluid streams hydrodynamically focus the sample fluid stream along the width and depth of the channel near to the bottom wall. The 3D hydrodynamically focused stream consisting of cells and particles was visualized in holographic mode using the inverted DHM microscope equipped with a 20× objective and a CMOS camera, as shown in the picture of the actual setup in figure 4(b). In our experiments of imaging and classification of cells and particles from the mixture, presented in figures 5(a)–(c), we chose $Q_s = 1\,\mu l\,min^{-1}$, $Q_{sh} = 40\,\mu l\,min^{-1}$ as suggested by the numerical simulations.

To demonstrate the overall operation of the microfluidic device, in figure 5(a) we show a snapshot of 3D hydrodynamic focusing of unstained cells, captured using a bright-field microscope with 10× objective. The 10× objective was used to demonstrate 3D hydrodynamic focusing with a wider field of view. Upstream of the junction, most of the cells appear out of focus as they are distributed throughout of depth of the channel. However, all the cells remain in the

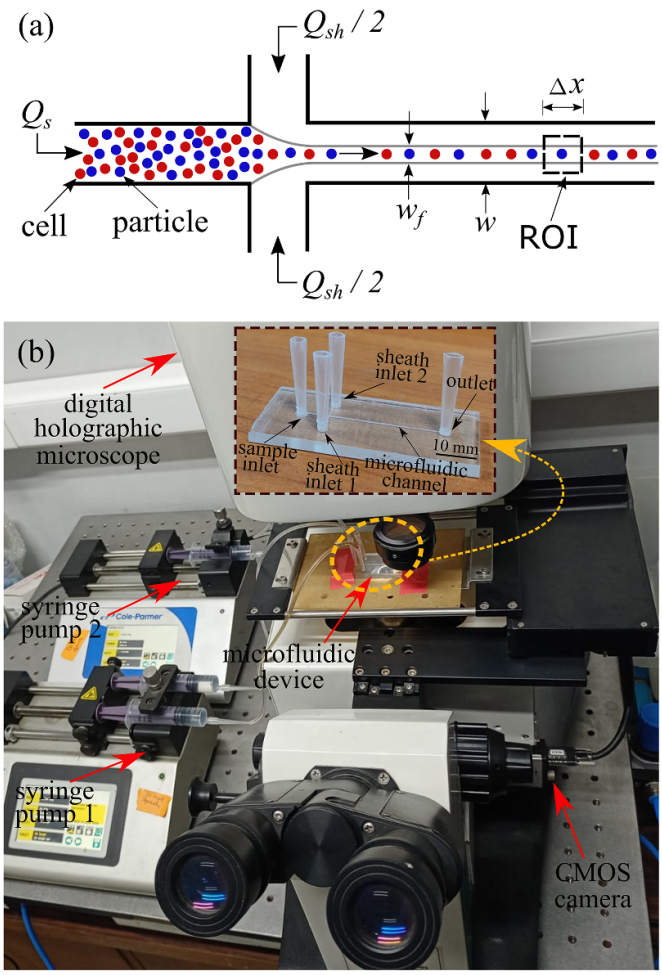

Figure 4. (a) Schematic illustration of the experiments to visualize and accurately classify cells and particles from a mixture using the combination of DHM and the 3D-hydrodynamic focusing device. (b) The actual experimental setup showing the various components of the setup. Inset of figure (b) shows the fabricated 3D flow focusing device.

focus of the microscopic objective downstream of the junction because RBCs flow in a single file after 3D hydrodynamic focusing. The 3D focusing of cells in a single file not only allows imaging of all the cells in a single focal plane but also prevents cell-clustering observed in previous works on DHM-based IFC [21, 22]. Additionally, we used a hologram domain criterion of least amplitude modulation of interference fringes [26], to ensure that the focus plane of the microscope objective lens nominally coincided with the hydrodynamic focus plane of our device. Therefore, image reconstruction using DHM in our experiments did not require numerical refocusing along the depth of the microchannel.

For cell and particle classification experiments, we selected a small ROI downstream of the junction (350 μm × 36 μm), as all the cells and/or particles flow in a single file, as schematically illustrated in figure 4(a) and observed experimentally in figure 5(a). To image all the cells and particles, it is necessary to choose the camera's frame rate ($1/\Delta t$) such that no cell passes the ROI during the time interval (Δt) between acquiring two successive images. This criterion can be fulfilled if

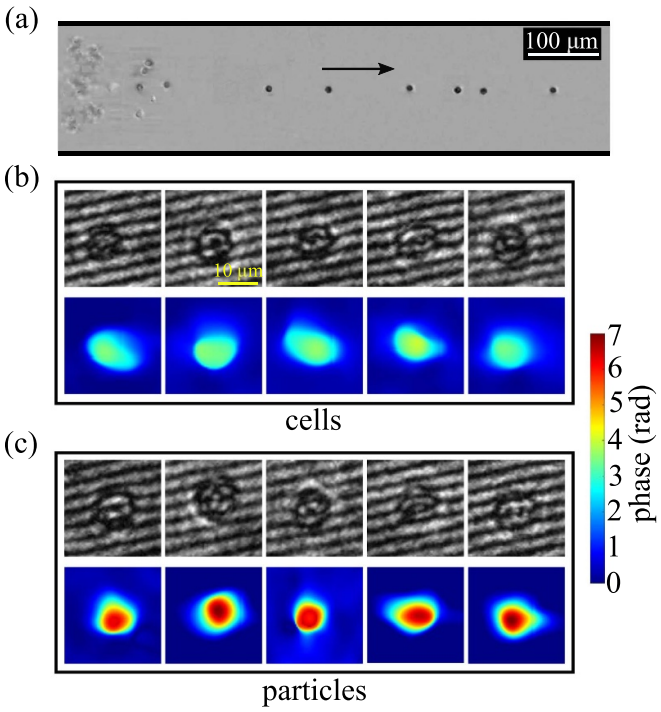

Figure 5. (a) Demomstration of 3D-hydrodynamic focusing in the microfluidic device using a low-magnification (10×) objective of brightfield microscope. All the cells remain in the optical focus of the microscopic objective downstream of the junction as cells flow in a single file after 3D focusing. (b), (c) Interference patterns and corresponding reconstructed phase images of five moving cells and particles acquired downstream of the junction using DHM with a 20× objective. The reconstructed phase value of particles is noticeably higher than that of cells, enabling classification.

Δt is less than the residence time ($\Delta x/\bar{u}$) of cells or particles within the ROI. Here, Δx is the axial length of ROI, and $\bar{u} = (Q_s+Q_{sh})/(wd)$ is the mean flow velocity in the sample channel. In our experiments, the $\Delta t = 9.5$ ms was chosen to be less than the residence time of 10.2 ms. Thus, in our experiments, the probability of missing the imaging of cells within the ROI is very low. We captured the interference patterns of cells and particles within the ROI, and from them, the phase profiles were generated by applying an optimization algorithm of Singh and Khare [25]. The five representative interference patterns and the corresponding phase reconstructed images of moving cells and particles are shown in figures 5(b) and (c), respectively. Note that all phase reconstructions were performed without applying the numerical refocusing algorithm.

2.4. Imaging of cells and particles

We performed four sets of experiments in which the first two sets consisted of flowing and imaging either cells or particles, while the third and fourth sets involved a sample mixture of cells and particles. The first and second sets of experiments were performed to check the typical maximum phase value of cells and particles, based on which we can classify the cells and particles from the mixture. Figures 6(a) and (c) present the temporal variation of the maximum phase, within the ROI, as individual cells and particles, respectively, flow one-by-one through the detection section. Each short (red) peak represents the presence of cells, while the tall (blue) peak represents the presence of particles within the detection section. The maximum phase value varies between 3.0–4.0 rad in individual cell experiments and 6.3–7.0 rad for individual particle experiments, as depicted in figures 6(a) and (c). In all, we imaged and counted 196 cells and 203 particles in experiments for individual cells and particles.

Figures 6(a) and (c) show the time instances at which the cells and particles arrive at the detection section, and the distribution of corresponding inter-arrival times. To determine whether all the cells and particles traveling through the detection section were imaged individually within the ROI, we plot the histogram of inter-arrival times in figures 6(b) and (d). The histograms of inter-arrival time reveal that the inter-arrival time follows an exponential distribution, which is typical of events that occur constantly and independently at a fixed mean rate. In the present case, these independent events are the arrival of cells and/or particles inside the ROI. The mean inter-arrival time for individual cells and particles experiments obtained by fitting an exponential distribution to the data for inter-arrival time is 0.31 s and 0.30 s, respectively. Because the mean inter-arrival time is much larger than the time interval between successive images ($\Delta t = 9.5$ ms), the probability of arrival of more than one cell together in ROI is very low.

Next, the third set of experiments was carried out in which the sample fluid consisted of a mixture of cells and particles, approximately in equal proportion. The temporal variation of the maximum phase, within the ROI, as the mixture of cells and particles flow one-by-one through the detection section, is shown in figure 6(e). In figure 6(e), the short (red) peaks correspond to the presence of cells, and the tall (blue) peaks are for the particles. There is a significant difference in the phase for cells and particles, which allows the classification of cells and particles from the mixture based on their maximum phase value. Figure 6(f) depicts that the inter-arrival time for the mixture of cells and particles case is also exponentially distributed like the experiments for individual cells and particles, and the mean inter-arrival time is 0.31 s. The throughput of our microfluidic holographic cytometry was 200 cells min^{-1}. Note that, in our approach, the throughput is limited by the camera frame rate, which was 105 fps in our experiments. The throughput can be easily scaled to order 2000 cells min^{-1} using commercially-available microscopy cameras with order 1000 fps frame rate and ten-fold higher sample and sheath flow rates.

2.5. Counting and classification of cells and particles from the mixture

In figure 7, we present the empirical distribution of the reconstructed phase values for DHM-IFC experiments for

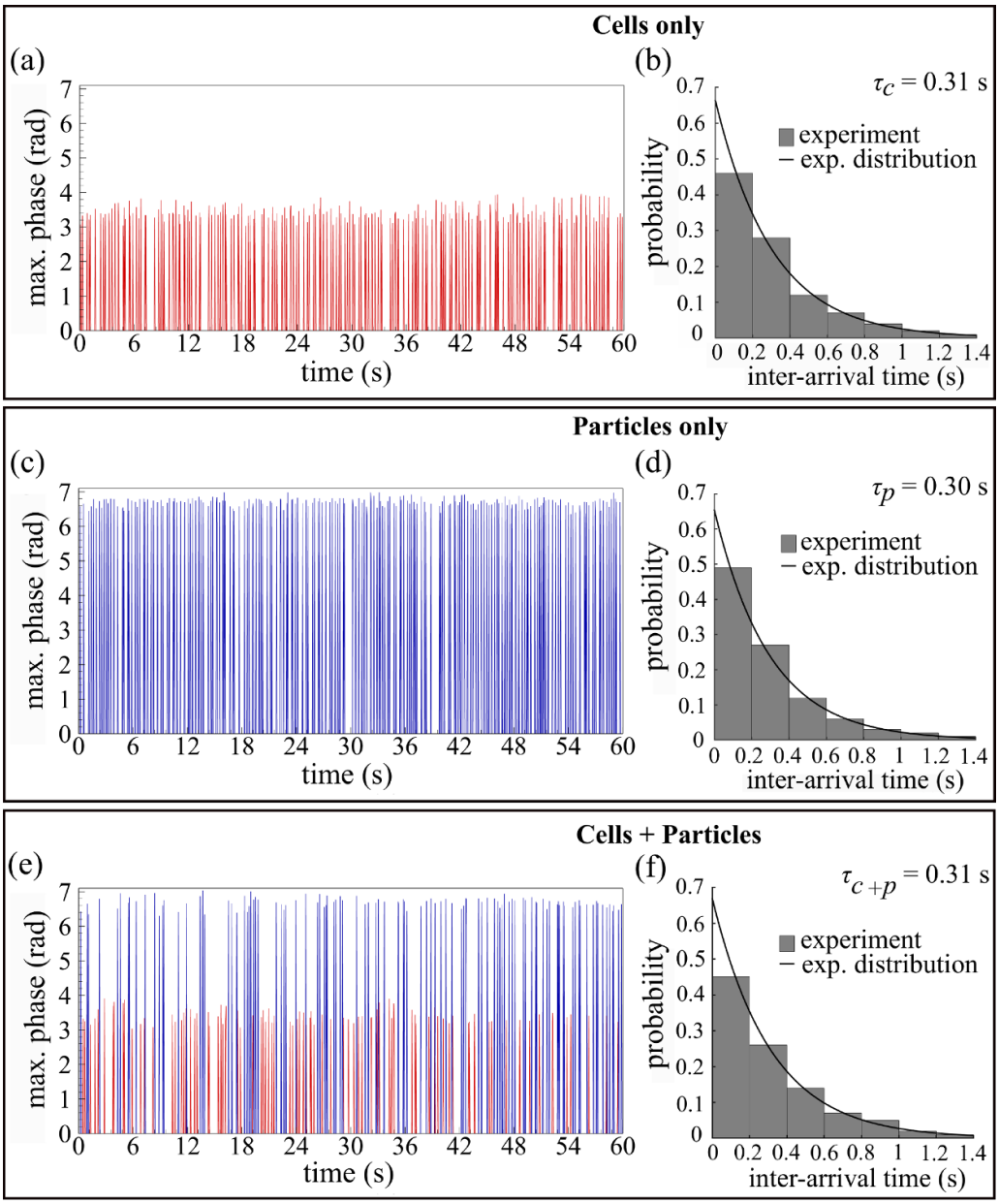

Figure 6. Temporal variation of maximum phase value for cells, particles, and the mixture of cells and particles (c : p = 50% : 50%) and the corresponding probability distribution of inter-arrival time. (a), (c) and (e) show the variation in maximum phase value within the ROI with time for cells, particles, and a mixture of cells and particles. The short (red) peak represents the presence of cells, whereas the tall (blue) peak speaks for particles. (b), (d) and (f) show the empirical distribution of inter-arrival times for cells, particles, and a mixture of cells and particles. The probability distribution of inter-arrival time is exponentially distributed, with a mean of 0.31 s for cells, 0.30 s for particles, and 0.31 s for the mixture of cells and particles.

individual cells, particles, and a mixture of cells and particles. Figure 7(a) corresponds to the individual cells and particles experiments in which the red color histogram between 3.0–4.0 rad shows the distribution of phase values for cells while the blue histogram between 6.3–7.0 rad corresponds to the particles. From figure 7(a), we infer that the difference in the mean phase value for cells and particles is much larger than the individual variability in phase value for the cells and particles. This statistically significant difference in the maximum phase value allows us to accurately classify cells and particles from the mixture. Figure 7(b) shows the histogram of phase values for the mixture of cells and particles in which cells and particles are mixed in roughly equal proportions. We counted 87 cells and 105 particles in a single experimental run. We then varied the proportion of cells and particles in the mixture to demonstrate that our method could accurately count and classify cells and particles from a mixture. To this end, we increased the relative proportion of cells by a factor of 1.6. Figure 7(c) shows the histogram of phase values for the mixture of cells and particles in which the proportion of cells and particles is 80%: 20%. We counted 142 cells and 43 particles in a single experimental run for this set

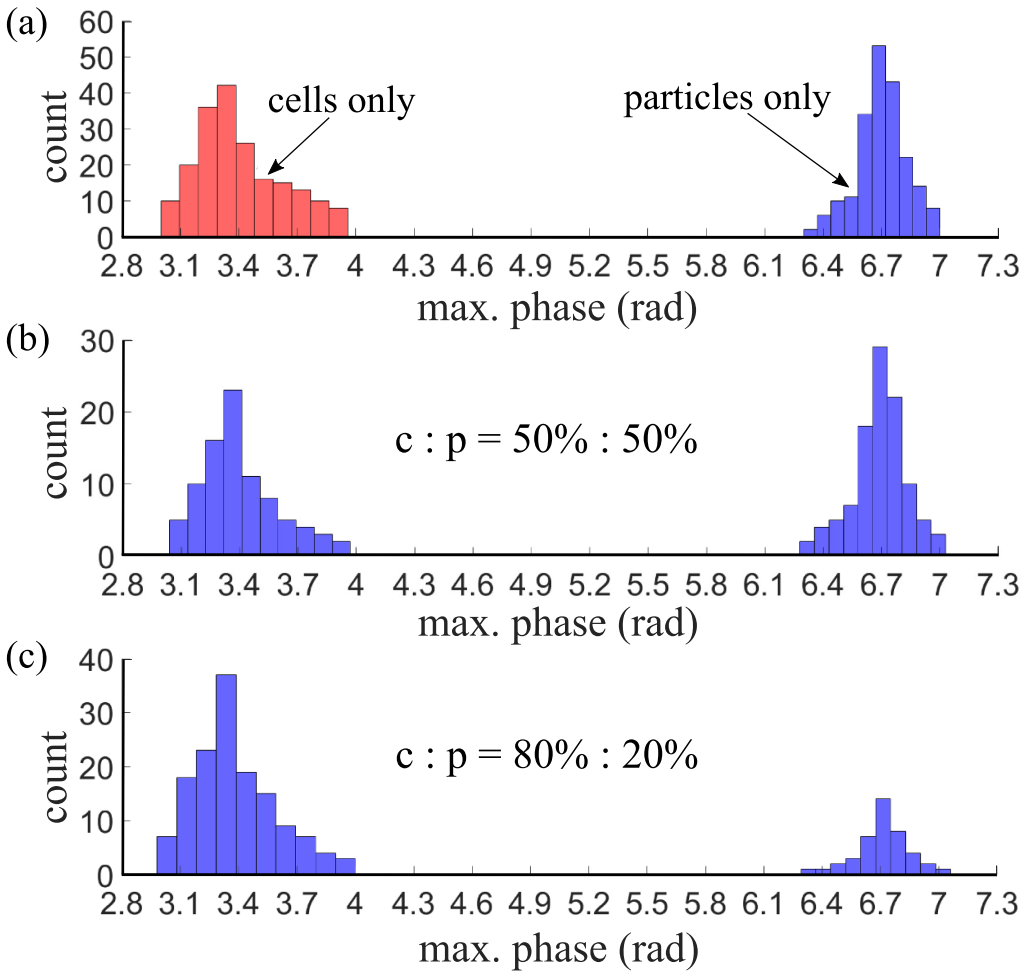

Figure 7. Counting or classification of cells and particles based on the maximum phase value in the ROI. (a) The red histogram shows the empirical distribution of maximum phase values for individual cell experiments, while the blue histogram corresponds to the particles. The 196 cells pass through detection volume in 60 s, having phase values in the range of 3.0–4.0 rad, whereas 203 particles cross the detection volume in 60 s, having phase values between 6.3 and 7.0 rad. (b), (c) Histogram of phase values for the mixture having 50% : 50% and 80% : 20% of cells and particles in the sample.

of experiments. The measured ratio of the number of cells to particles varies according to the change in sample composition fixed during the sample preparation, which demonstrates the ability of our approach to accurately count and classify each cell and particle in the mixture.

3. Conclusions

We have demonstrated an accurate holographic cytometry method using three-dimensional hydrodynamic focusing to visualize and classify cells and particles from a mixture. In contrast to the existing approaches, combining the 3D hydrodynamic focusing device with DHM allows accurate counting and classification of cells without the need for computationally-expensive numerical refocusing and complicated microfabrication processes. In this paper, we first demonstrated the ability of DHM for the classification of stationary RBCs and polystyrene particles which are otherwise indistinguishable in brightfield and phase-contrast microscopy. Using DHM, we classified the cells and particles on the basis of reconstructed phase values, and the maximum phase for cells and particles ranges between 3.0–4.0 rad and 6.3–7.0 rad, respectively. Next, we have presented visualization and classification of flowing cells and particles in an inexpensive 3D hydrodynamic focusing microfluidic device using DHM. Our experiments clearly show that DHM along with the 3D focusing device can perform accurate, label-free classification and quantification of cells and particles in IFC. In the future, we plan to explore the use of DHM-based IFC for cell classification in practical applications such as disease diagnostics, cancer research, and genomics.

Data availability statement

All data that support the findings of this study are included within the article (and any supplementary files).

Acknowledgment

We acknowledge the financial support received from the Department of Science and Technology, Ministry of Science and Technology, Government of India (Grant/Award Number ID/MED/34/2016).

Conflict of interest

There are no conflicts to declare.

ORCID iDs

Yogesh M Patel https://orcid.org/0000-0001-8500-7014
Kedar Khare https://orcid.org/0000-0002-3104-3850
Supreet Singh Bahga https://orcid.org/0000-0001-7277-9015

References

[1] Grimwade L F, Fuller K A and Erber W N 2017 *Methods* **112** 39–45
[2] Doan M, Vorobjev I, Rees P, Filby A, Wolkenhauer O, Goldfeld A E, Lieberman J, Barteneva N, Carpenter A E and Hennig H 2018 *Trends Biotechnol.* **36** 649–52
[3] Stavrakis S, Holzner G, Choo J and DeMello A 2019 *Curr. Opin. Biotechnol.* **55** 36–43
[4] Samsel L, Dagur P K, Raghavachari N, Seamon C, Kato G J and McCoy Jr J P 2013 *Cytometry* B **84** 379–89
[5] Han Y, Gu Y, Zhang A C and Lo Y-H 2016 *Lab Chip* **16** 4639–47
[6] Basiji D A, Ortyn W E, Liang L, Venkatachalam V and Morrissey P 2007 *Clin. Lab. Med.* **27** 653–70
[7] Schonbrun E, Gorthi S S and Schaak D 2012 *Lab Chip* **12** 268–73
[8] Hur S C, Tse H T K and Di Carlo D 2010 *Lab Chip* **10** 274–80
[9] Rane A S, Rutkauskaite J, deMello A and Stavrakis S 2017 *Chem* **3** 588–602
[10] Diebold E D, Buckley B W, Gossett D R and Jalali B 2013 *Nat. Photon.* **7** 806–10
[11] Han Y and Lo Y H 2015 *Sci. Rep.* **5** 1–10
[12] Wang G and Fang N 2012 *Methods Enzymol.* **504** 83–108
[13] Kemper B *et al* 2019 Label-free quantitative *in vitro* live cell imaging with digital holographic microscopy *Label-Free Monitoring of Cells In Vitro* (*Bioanalytical Reviews*) (Berlin: Springer) pp 219–72
[14] Kemper B and Von Bally G 2008 *Appl. Opt.* **47** A52–A61
[15] Kim M K 2011 *Digital Holographic Microscopy* (Berlin: Springer)
[16] Zetsche E-M, El Mallahi A, Dubois F, Yourassowsky C, Kromkamp J C and Meysman F J R 2014 *Limnol. Oceanogr. Methods* **12** 757–75
[17] Mandracchia B, Bianco V, Wang Z, Mugnano M, Bramanti A, Paturzo M and Ferraro P 2017 *Lab Chip* **17** 2831–8
[18] Xin L, Xiao W, Che L, Liu J, Miccio L, Bianco V, Memmolo P, Ferraro P, Li X and Pan F 2021 *ACS Omega* **6** 31046–57
[19] Zhang Y, Wang H, Wu Y, Tamamitsu M and Ozcan A 2017 *Opt. Lett.* **42** 3824–7
[20] Zimmerman T, Duong J K, Dean Z, Bianco S and Esquerra R 2022 Evaluating automated reconstruction methods for digital inline holographic images of plankton *Proc. SPIE* **12026** 26–36
[21] Chen C X, Park H S, Price H and Wax A 2021 *Front. Phys.* **9** 688
[22] Park H-S, Price H, Ceballos S, Chi J-T and Wax A 2021 *Cells* **10** 2455
[23] Mangal J, Monga R, Mathur S R, Dinda A K, Joseph J, Ahlawat S and Khare K 2019 *J. Biophoton.* **12** e201800409
[24] Pandey N, Ghosh A and Khare K 2016 *Appl. Opt.* **55** 2418–25
[25] Singh M and Khare K 2018 *J. Mod. Opt.* **65** 1127–34
[26] Malik R, Sharma P, Poulose S, Ahlawat S and Khare K 2020 *J. Microsc.* **279** 114–22